Rational Design of Efficient Palladium Catalysts for Electroreduction of Carbon Dioxide to Formate

Anna Klinkova,[†,∥] Phil De Luna,[‡,∥] Cao-Thang Dinh,[§] Oleksandr Voznyy,[§] Egor M. Larin,[†] Eugenia Kumacheva,*[,†] and Edward H. Sargent*[,§]

[†]Department of Chemistry, University of Toronto, Toronto, Ontario M5S 3H6, Canada
[‡]Department of Materials Science & Engineering, University of Toronto, 184 College Street, Toronto, Ontario M5S 3E4, Canada
[§]The Edward S. Rogers Sr. Department of Electrical and Computer Engineering, University of Toronto, 10 King's College Road, Toronto, Ontario M5S 3G4, Canada

ⓢ *Supporting Information*

ABSTRACT: The electrochemical reduction of CO_2 into renewable chemical products such as formic acid is an important and challenging goal. Traditional Pd catalysts suffer from CO poisoning, which leads to current density decay and short operating lifetimes. Here we explored the ability to control Pd nanoparticle surface morphology to amplify catalytic activity and increase stability in the electroreduction of CO_2 to formate. Through computational studies we have elucidated trends in intermediate binding which govern the selectivity and catalytic activity. We then rationally synthesized Pd nanoparticles having an abundance of high-index surfaces to maximize electrocatalytic performance. This catalyst displays a record current density of 22 mA/cm^2 at a low overpotential of −0.2 V with a Faradaic efficiency of 97%, outperforming all previous Pd catalysts in formate electrosynthesis. The findings presented in this work provide rational design principles which highlight morphological control of high-index surfaces for the effective and stable catalytic electroreduction of CO_2 to liquid fuels.

KEYWORDS: *carbon dioxide, palladium, nanoparticle, shape, facet, electrochemical CO_2 reduction*
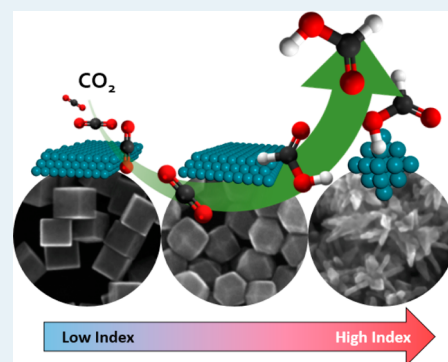
■ INTRODUCTION

The electrochemical conversion of carbon dioxide (CO_2) into synthetic fuels and value-added chemicals is a key enabler of carbon-neutral energy sources, since it provides a means to store renewable electricity in a high-density (energy per volume) liquid form.[1] Unfortunately, CO_2 electoreduction suffers from a high overpotential, poor product selectivity, and insufficient electrocatalyst stability.[1,2] The field seeks stable electrode materials that efficiently and selectively reduce CO_2 to useful products at low overpotentials.

Electroreduction of CO_2 into formic acid is of particular interest, as formic acid can be used as a fuel in direct formic acid fuel cells[3] and is used today in the synthesis of fine chemicals such as pharmaceuticals[4,5] and as a preservative and antibacterial agent.[6] Formate and formic acid are the main products of CO_2 electroreduction on post transition metals, such as Pb, Hg, Tl, In, Sn, Cd, and Bi; however, previously reported electroreduction studies using these materials have required very negative potentials relative to the equilibrium potential to achieve good product selectivity.[7,8] Among inorganic strategies, only through the use of Pd electroreduction of CO_2 to formate have potentials close to the equilibrium potential been obtained; indeed, these results come impressively close to the performance of formate dehydrogenase enzymes.[9]

Currently, Pd nanoparticles (NPs) used in the selective reduction of CO_2 to formate have been limited to low current densities: specifically, only sub-mA/cm^2 geometric current densities have been reported at near-equilibrium potential.[10,11] Recently, Pd NP-based electrocatalysts with near-quantitative Faradaic efficiency, impressive geometric current densities (10 mA/cm^2 at −0.2 V in 2.8 M KHCO$_3$), and high mass activity have been reported for CO_2 reduction to formate.[12]

In these otherwise very promising studies, one key challenge remains: over the course of the reaction, performance was lost.[12] Thus, although the application of Pd NPs shows great promise for energy-efficient electroreduction of CO_2, further understanding has to be developed for the factors that affect their stability and high selectivity.
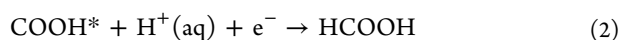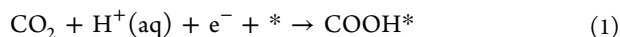
It has been proposed that the reduction of stability of Pd nanocatalysts in formate synthesis originates from CO poisoning.[12] While at high overpotentials CO_2 steadily reduces to CO, at low overpotential, CO is only forming in trace amounts and yet this is sufficient for catalyst surface poisoning.[13] Two proposed multistep mechanisms of electrochemical reduction of CO_2 to formic acid include the following.

Mechanism 1:

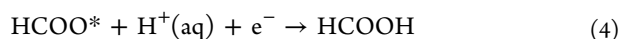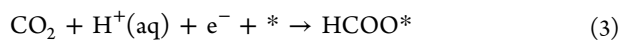$$CO_2 + H^+(aq) + e^- + * \rightarrow COOH* \qquad (1)$$

$$COOH* + H^+(aq) + e^- \rightarrow HCOOH \qquad (2)$$

Mechanism 2:

$$CO_2 + H^+(aq) + e^- + * \rightarrow HCOO* \qquad (3)$$

$$HCOO* + H^+(aq) + e^- \rightarrow HCOOH \qquad (4)$$

Additionally, the competing electrochemical reduction of CO_2 to CO proceeds as follows:

$$COOH*/HCOO* + H^+(aq) + e^- \rightarrow CO* + H_2O \qquad (5)$$

$$CO* \rightarrow CO + * \qquad (6)$$
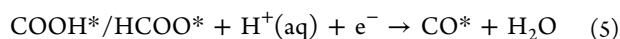
where * represents either a vacant surface catalytic active site or intermediate species adsorbed on the active site. The production of formic acid is proposed to proceed through either a proton/electron pair transfer to form a carboxyl (COOH*) (reaction 1) or a formate (HCOO*) intermediate (reaction 3). Next, the COOH* (reaction 2) or HCOO* (reaction 4) can be reduced to HCOOH with a subsequent proton/electron pair transfer. Importantly, reaction 5 leads to the formation of CO species bound to the active site: this in turn poisons the surface of the catalyst.[9,12] Furthermore, it has previously been shown that the more favored intermediate for CO evolution is COOH*.[17]

The surface of the electrode can be reactivated by short oxidative treatment.[12] More desirably, though, CO poisoning would be reduced, and the selectivity toward formic acid synthesis, by designing a catalyst that would stabilize the formation of intermediates that reduce to HCOOH (steps 1−4) and inhibit the formation of intermediate bound CO (steps 5 and 6).

Here we focus on designing the surface of the metal surface to weaken the CO binding affinity. We contemplate either varying the size of NPs or honing the arrangement of atoms on their facets. The difference in surface atomic arrangements results in different stabilization energies of the reaction intermediate,[14] an effect that is specific for a particular metal material. The effect of metal surface morphology on CO_2 electroreduction pathways and efficiencies has been reported for gold and copper NPs.[14,15] It has been established that low-coordinated sites on gold NPs favor the formation of carbon monoxide,[15] while copper NPs exhibit increased catalytic activity and selectivity with decreasing NP size.[16] Recently, it has been shown that the Pd NP size influences Faradaic efficiencies of CO_2 to CO electroreduction in the potential range from 0.6 to −1.2 V (vs RHE), which was also attributed to the higher efficiency of edge sites, in comparison to terrace sites.[17] To the best of our knowledge, no comprehensive studies have been conducted to explore the effect of Pd NP morphology on CO_2 electroreduction to formate catalyzed by Pd NPs.

We begin by elucidating the underlying principles in the morphology-governed catalytic performance of Pd NPs. We seek to do this by carrying out density functional theory (DFT) studies of Pd(111), Pd(110), Pd(100), and Pd(211) NP surfaces and a Pd_{19} cluster, revealing the relation between the surface atomic coordination and the catalytic behavior of NPs in CO_2 electroreduction. Following the theoretical predictions, we designed and synthesized a family of Pd NPs with various

shapes and enclosing surface planes, for which we explored electrocatalytic performance in the CO_2 reduction reaction. Our work shows favorably high intrinsic catalytic CO_2 electroreduction activity and stability on branched Pd NPs, enclosed by high-index facets and surface kinks, in comparison with other types of Pd NPs. The best catalysts achieve impressive Faradaic efficiencies (FE > 90%) and exceptionally high current density (~15 mA/cm^2), both realized at low overpotentials (−0.2 V vs RHE). In summary, we have leveraged morphology-driven principles to maximize electrocatalytic efficiency and stability by rationally designing Pd NPs with sharp geometric features.

■ RESULTS AND DISCUSSION

Recent DFT screening of metal surfaces and facets for formic acid synthesis showed that there is a high probability the reaction takes place with the HCOO* intermediate.[18] Furthermore, these studies showed that Pd had the lowest limiting potential, closely matching the equilibrium potential for the synthesis of formic acid. Being inspired by these findings, we performed a series of DFT calculations on Pd surfaces to explore the relationship between a specific surface facet and catalytic electroreduction of CO_2 to formic acid. In these studies, we elucidated the thermodynamic reaction energy barriers and free energies of formation for the reaction intermediates (HCOO*, CO*, COOH*) on different facets. The catalyst surfaces were modeled with the Vienna ab initio simulation package (VASP)[19] with periodic boundary conditions using the atomic simulation environment (ASE)[20] (see the Supporting Information).

To identify the most favored reaction intermediate during the first proton-coupled electron transfer step, we calculated the electronic binding energies of HCOO* vs COOH* intermediates on Pd(111), Pd(100), Pd(110), and Pd(211) planes, as well as on the Pd_{19} cluster (Table S3 in the Supporting Information). We found that the binding energy of COOH* was more negative on low-index facets Pd(111) and Pd(100), whereas the binding energy of HCOO* was more negative on high-index facets Pd(110) and Pd(211). For example, the binding energies of COOH* and HCOO* on the stepped Pd(211) surface were −0.35 and −0.42 eV, respectively. The more negative binding energy of the HCOO* intermediate suggested that the reaction proceeds via a formate rather than a carboxyl intermediate, in agreement with recently published results.[18] Conversely, Pd(111) and Pd(100) surfaces favored the COOH* intermediate, which is more likely to lead to CO poisoning.

Next, the electronic energies of HCOO* on Pd(111), Pd(110), Pd(100), Pd(211), and Pd_{19} surfaces were converted into the free energies (ΔG) of the bound intermediates at 298 K, 1 atm, and pH 0 at 0 V vs the reverse hydrogen electrode (RHE) (Table S4 in the Supporting Information). Figure 1 shows the free energy diagram of CO_2 calculated using the computational hydrogen electrode model.[21] The ΔG_{max} values for CO and HCOOH production via COOH* and HCOO* were also calculated for pH 0 and 7.2 (Table S4).

When the Pd surface contained higher-index facets with more steps and undercoordinated atoms, the energy barrier associated with the catalytic reaction (ΔG) decreased. Thus, on the basis of Figure 1, the structures with more steps, edges, and grain boundaries are expected to exhibit a greater catalytic activity. The Pd_{19} cluster was included in the study as an
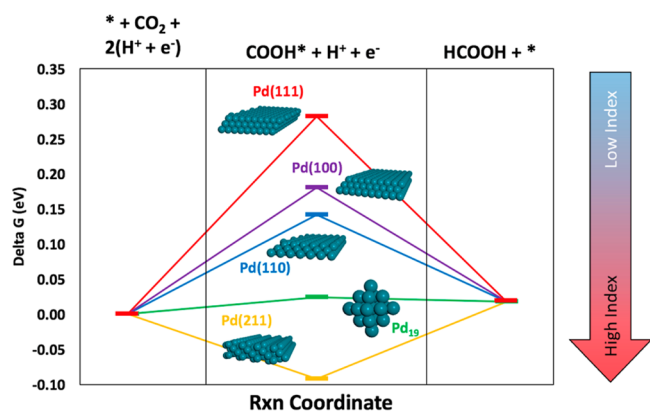
Figure 1. (left) Free energy diagrams for the electrochemical reduction of CO_2 to formic acid on Pd(111) (red), Pd(100) (blue), Pd(110) (purple), Pd(211) (green), and Pd$_{19}$ cluster (yellow). The reaction energy barrier is significantly decreased as the index increases. (right) Free energies of CHOO* and CO* intermediates on Pd(111), Pd(100), Pd(110), Pd(211), and Pd$_{19}$. As the surface index increases, the CO* intermediate is destabilized while the COOH* intermediate is stabilized. This suggests that sharper features are less susceptible to CO poisoning while simultaneously promoting formic acid production. The reaction energy barriers for CO and HCOOH production via the COOH* and HCOO* intermediates are summarized in Table S5 in the Supporting Information.

approximation for adatoms, surface defects, or undercoordinated sites that may be present.

Additionally, the {211} plane has found to have the lowest energy barrier and is thus thermodynamically the most favorable surface termination for the reaction to proceed. As a result, this plane usually exhibits the highest catalytic activity: e.g., as has been shown for CO_2 electroreduction on gold.[14]

In order to explore the effect of surface morphology of Pd on CO poisoning, we compared the free energies of formation, $\Delta G_{formation}$, of HCOO* and CO* intermediates to the surface: that is, the free energy of reactions 3 ($CO_2 + H^+(aq) + e^- + * \rightarrow HCOO*$) and 5 (COOH*/HCOO* + $H^+(aq) + e^- \rightarrow CO* + H_2O$) as shown above. Figure 2 shows the variation in the value of $\Delta G_{formation}$ of CO* and HCOO* to different surface facets. We found that for CO* the value of $\Delta G_{formation}$ increases from −0.83 eV (Pd(111)) to −0.65 eV (Pd(211)), whereas for HCOO*, the value of $\Delta G_{formation}$ decreases from 0.28 (Pd(111)) to −0.09 eV (Pd(211)) These results suggest

that the formation of CO* on Pd surfaces is less favored with increasing index, thus decreasing CO binding, while the formation of HCOO* becomes more favored.

Next, charge density and d orbital analyses of Pd were performed to probe how the change in surface facet affects the binding of intermediates to the Pd surface. To this end, we have calculated Bader partial atomic charges[22] (Table S6 in the Supporting Information) and projected density of states (PDOS) for the binding site Pd d orbitals, as shown in Figure 3. The Bader charges show that as the surface index increases the charge density on the Pd atom bound to CO decreases while the Pd atom bound to HCOO increases. This change in charge density implies that the Pd−HCOO* bond is strengthened whereas the Pd−CO* bond is weakened. Furthermore, the PDOS for the Pd d orbital shows an increase in the peak around −0.3 eV on Pd(211), whereas there is no change in the highest energy peak for Pd(111). This suggests that on the Pd(211) surface, when HCOO* is bound, there are a greater number of states closer to the Fermi level which are available for binding. Additional PDOS plots for Pd(110), Pd(100), and Pd$_{19}$ are shown in Figure S1 in the Supporting Information. The far-reaching implication of these results is that Pd NPs with sharper features may be less susceptible to CO poisoning *and* also simultaneously favor HCOOH production.

Following the predictions of DFT calculations, we developed high-index-faceted Pd catalysts for formate synthesis. We used large-scale synthesis of Pd NPs with specific shapes enclosed by various types of facets stabilized with cetyltrimethylammonium bromide.[23] More specifically, we synthesized {100} plane-enclosed nanocubes (NCs),[24,25] {110} plane-enclosed rhombic dodecahedra (RDs),[26] NPs with mixed low-index facets,[26] and branched NPs enclosed by high-index facets (BNPs).[27]

Figure 4a−d shows scanning electron microscopy (SEM) images of the NPs. The side length of the NCs was 42 ± 4 nm. For the RD and BNP NPs, the dimensions were defined as the diameters of circles that can fit these NPs: 71 ± 6 and 108 ± 11 nm, respectively. For these three NP types the shape purity was ≥95%, as determined from the SEM image analysis. The NPs with mixed low-index facets were represented by the faceted spheres with a diameter 74 ± 12 nm and the nanorods with dimensions (108 ± 19 nm) × (28 ± 4 nm). Commercial Pd black (99.95% purity, purchased from Sigma-Aldrich) with the smeared morphology and the size of small features below 20
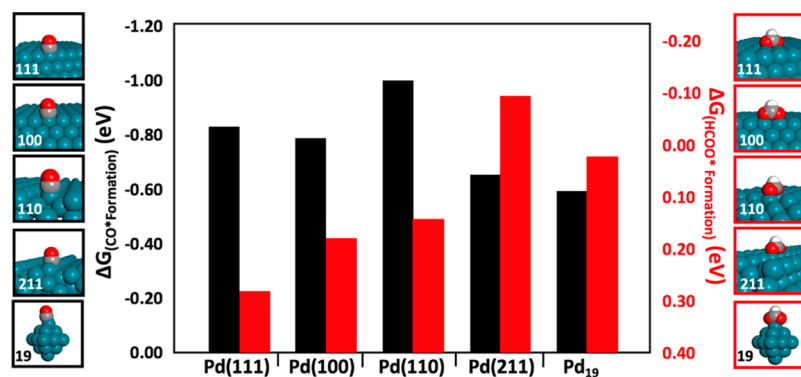
Figure 2. Free energies of formation for HCOO* and CO* intermediates on Pd(111), Pd(100), Pd(110), Pd(211), and Pd$_{19}$. The formation energy of the CO* intermediate is reduced while the formation energy of the HCOO* intermediate increases on higher index surfaces. This suggests that sharper features promote the formation of the HCOO* intermediate, which in turn promotes the production of HCOOH. The trend also shows that sharper features lead to a lower propensity for CO* production.
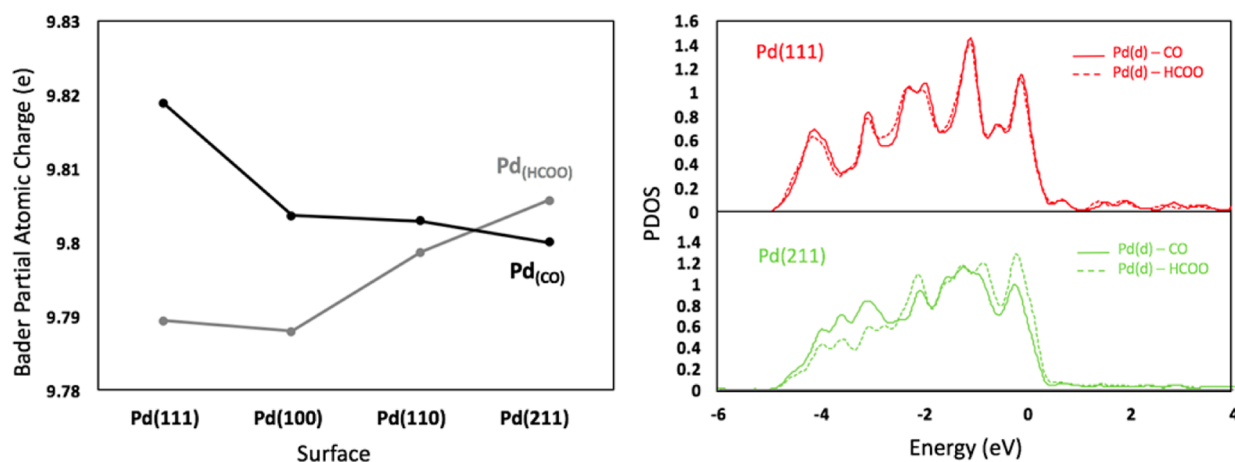
Figure 3. (left) Bader partial atomic charges for the Pd atom bound to the intermediates HCOO* and CO* as a function of surface facet. (right) Projected density of states (PDOS) Pd d orbitals. The Pd(111) bound to CO* (solid red line) and HCOO* (dashed red line) are shown at the top, and the Pd(211) bound to CO* (solid green line) and HCOO* (dashed green line) are shown at the bottom.
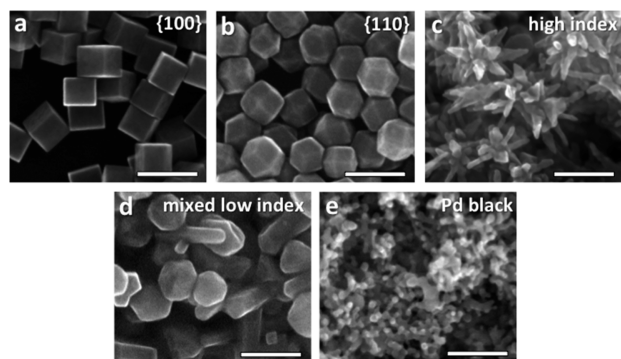
Figure 4. SEM images of Pd NPs used for electrode fabrication: NCs (a), RDs (b), BNPs (c), NPs with mixed low-index facets (d), and Pd black (e). Scale bar 100 nm.

nm was used as a control material. Since the {111} facet is the most thermodynamically stable, we assume that the control material has a high proportion of this facet exposed.[28] The NPs were deposited from the NP slurry in the methanol−water mixture on the carbon paper using Nafion (Supporting Information). The NPs densely covered the 0.6 cm × 0.6 cm area of the carbon paper, without carbon fiber exposed to the solution (Supporting Information).

Figure 5a shows the total geometric current densities for the catalysts prepared from different types of Pd NPs. At the beginning of electrolyses, the geometric current densities were increased from 15 to 22 mA/cm^{-2} (at −0.2 V overpotential). In the course of the reaction, the geometric current densities were reduced for all NPs studied. The decline of the current density was associated with CO poisoning of the nanocatalyst surface, and thus the rate of decline characterized NP stability in the electroreduction of CO$_2$. The rate of current density reduction increased in the raw BNPs, RDs, NCs, NPs with mixed low-index facets, and commercial Pd black. The trend in reduced NP stability was in agreement with the theoretically predicted relationship between the facets, enclosing the NPs and their binding energies for reaction intermediates. In particular, in DFT calculations we found that higher index facets had a lower binding energy of CO and higher binding energy of formate intermediate, which suggested that higher index facets were less susceptible to CO poisoning. Experimentally, we find the

lowest rate of current density decay for BNPs, which were enclosed by high-index facets, in agreement with our computational predictions.

Next, we quantified the FE of formate formation by determining formate concentration in the solution after a reaction time of 1 h. Formate was esterified to ethyl formate,[29] which allowed the measurement of its concentration using gas chromatography (GC). The values of FE in electrocatalytic formate synthesis were 97%, 95%, and 90% for BNPs and RDs, 95% for NCs, and 90% for NPs with mixed low-index facets and Pd black; the remainder of FE (<10%) was responsible for the hydrogen evolution reaction, while no CO presence was detected by GC.

The electrochemically active surface area (ECSA) of the electrodes was determined using a CO stripping method described elsewhere.[30] Figure 5b shows the CO stripping voltammograms recorded in 0.5 M H$_2$SO$_4$ solution. The broadening of the anodic CO oxidation peak for the BNP electrode was attributed to a variety of active sites in BNPs, caused by their complex high-index facet surface morphology. More narrow anodic CO oxidation peaks for all other electrodes were consistent with the more defined surface sites for the NPs forming these electrodes. The relative positions of the anodic current peaks for the electrodes comprised of NCs and RDs (enclosed by {100} and {110} facets, respectively) were in agreement with the relative current peak positions reported for the corresponding single-crystal Pd electrodes.[31] The ECSAs of the electrodes were calculated from the stripping voltammograms (Figure 5b) using the charge of 420 μC/cm^2 required for the removal of a monolayer of CO from Pd (Supporting Information).[32] Figure 5b shows the ECSA-normalized current densities for all types of the electrodes. The initial current density of the BNP electrode was significantly higher than that of electrodes comprised of other types of NPs with low-index facets, in agreement with the theoretically predicted trends (Figure 2).

To explore further the long-term performance of BNP electrodes, we examined their recovery by oxidative treatment[12] and compared it with the recovery of NC electrode. We performed 1 h electrolysis followed by 10 min long oxidative treatment of the electrode by exposing it to the air, after which the next electrolysis round was carried out. Although the initial performances of the BNP and NC electrodes were comparable,
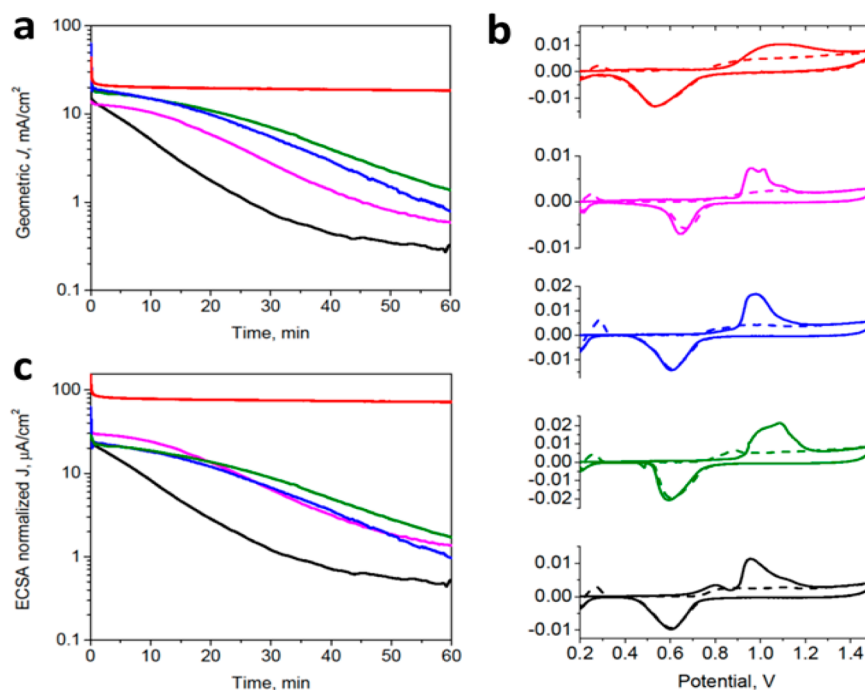
Figure 5. CO_2 electroreduction activity of different Pd NPs in 0.5 M $KHCO_3$ at −0.2 V: (a) geometric current densities; (b) CO stripping voltammograms on different Pd NPs. Color scheme: red, BNP; green, RDs; blue, NCs; magenta, NPs with mixed low index facets; black, Pd black. (c) ECSA normalized current densities.

a significantly higher current decay rate was observed for the NC electrode (Figure 6). The oxidative treatment resulted in
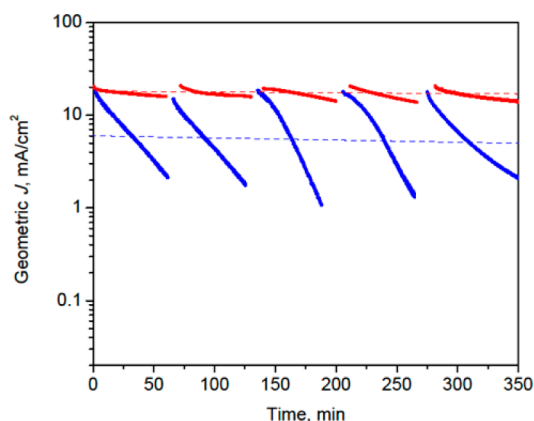
Figure 6. Stability of BNPs (red) and NCs (blue) in 0.5 M $KHCO_3$ at −0.2 V. The electrodes were exposed to air for 10 min between 1 h long CO_2 electroreduction runs. Dashed lines are shown as guides to the eye for the median geometric current densities across five electroreduction runs.

almost complete recovery of both BNP and NC electrodes, with a significantly (3-fold) higher average current density over five cycles for the BNP electrode.

■ CONCLUSION

In conclusion, we found herein that NPs with high-index facets suppress CO poisoning while simultaneously promoting formic acid synthesis. Computational simulations were utilized to study the intermediate binding energies of competing mechanisms with respect to changing morphology to promote the evolution of the preferred product while suppressing catalytic poisoning. We leveraged a new understanding of the role of the surface morphology of NPs to maximize their electrocatalytic performance. This has resulted in a catalyst with a record performance of 22 mA/cm^2 geometric current density at a low overpotential of −0.2 V and near-unity Faradaic efficiency. Fundamentally, our findings provide important insights into the rational design of catalysts for the selective and stable production of fuels from CO_2. In particular, our results underline the importance of high-index surfaces and morphological design of Pd NPs for their enhanced catalytic performance. These findings contribute to the goal of developing efficient catalysts for CO_2 reduction for the generation of renewable fuels and feedstocks.

■ ASSOCIATED CONTENT

Ⓢ Supporting Information

The Supporting Information is available free of charge on the ACS Publications website at DOI: 10.1021/acscatal.6b01719.

Computational details, experimental details, and additional SEM images (PDF)

■ AUTHOR INFORMATION

Corresponding Authors

*E-mail for E.K.: ekumache@chem.utoronto.ca.
*E-mail for E.H.S.: ted.sargent@utoronto.ca.

Author Contributions

‖These authors contributed equally to this work.

Notes

The authors declare no competing financial interest.

■ ACKNOWLEDGMENTS

■ REFERENCES

(1) Whipple, D. T.; Kenis, P. J. A. *J. Phys. Chem. Lett.* **2010**, *1*, 3451−3458.

(2) Hu, B.; Guild, C.; Suib, S. L. *J. CO2 Util.* **2013**, *1*, 18−27.

(3) Yu, X.; Pickup, P. G. *J. Power Sources* **2008**, *182*, 124−132.

(4) Szmant, H. *Organic Building Blocks of the Chemical Industry*; Wiley: New York, 1989.

(5) Mura, M. G.; De Luca, L.; Giacomelli, G.; Porcheddu, A. *Adv. Synth. Catal.* **2012**, *354*, 3180−3186.

(6) Hietala, J., Vuori, A., Johnsson, P., Pollari, I., Reutemann, W.; Kieczka, H. *Formic Acid. Ullmann's Encyclopedia of Industrial Chemistry*; Wiley: New York, 2016; pp 1−22.

(7) Chaplin, R. P. S.; Wragg, A. A. *J. Appl. Electrochem.* **2003**, *33*, 1107−1123.

(8) Zhang, S.; Kang, P.; Meyer, T. J. *J. Am. Chem. Soc.* **2014**, *136*, 1734−1737.

(9) Armstrong, F. a; Hirst. *Proc. Natl. Acad. Sci. U. S. A.* **2011**, *108*, 14049−14054.

(10) Stalder, C. J.; Chao, S.; Wrighton, M. S. *J. Am. Chem. Soc.* **1984**, *106*, 3673−3675.

(11) Podlovchenko, B. I.; Kolyadko, E. A.; Lu, S. G. *J. Electroanal. Chem.* **1994**, *373*, 185−187.

(12) Min, X.; Kanan, M. W. *J. Am. Chem. Soc.* **2015**, *137*, 4701−4708.

(13) Hori, Y.; Wakebe, H.; Tsukamoto, T.; Koga, O. *Electrochim. Acta* **1994**, *39*, 1833−1839.

(14) Zhu, W.; Michalsky, R.; Metin, O.; Lv, H.; Guo, S.; Wright, C. J.; Sun, X.; Peterson, A. A.; Sun, S. *J. Am. Chem. Soc.* **2013**, *135*, 16833−16836.

(15) Mistry, H.; Reske, R.; Zeng, Z.; Zhao, Z.-J.; Greeley, J.; Strasser, P. *J. Am. Chem. Soc.* **2014**, *136*, 16473−16476.

(16) Reske, R.; Mistry, H.; Behafarid, F.; Cuenya, B. R.; Strasser, P. *J. Am. Chem. Soc.* **2014**, *136*, 6978−6986.

(17) Gao, D.; Zhou, H.; Wang, J.; Miao, S.; Yang, F.; Wang, G.; Wang, J.; Bao, X. *J. Am. Chem. Soc.* **2015**, *137*, 4288−4291.

(18) Yoo, J. S.; Christensen, R.; Vegge, T.; Norskøv, J. K.; Studt, F. *ChemSusChem* **2016**, *9*, 358−363.

(19) Kresse, G.; Furthmüller, J. *Phys. Rev. B: Condens. Matter Mater. Phys.* **1996**, *54*, 11169.

(20) Bahn, S. R.; Jacobsen, K. W. *Comput. Sci. Eng.* **2002**, *4*, 56−66.

(21) Norskøv, J. K.; Rossmeisl, J.; Logadottir, A.; Lindqvist, L.; Kitchin, J. R.; Bligaard, T.; Jonsson, H. *J. Phys. Chem. B* **2004**, *108*, 17886−17892.

(22) Tang, W.; Sanville, E.; Henkelman, G. *J. Phys.: Condens. Matter* **2009**, *21*, 084204.

(23) Klinkova, A.; Larin, E. M.; Prince, E.; Sargent, E. H.; Kumacheva, E. *Chem. Mater.* **2016**, *28*, 3196−3202.

(24) Niu, W.; Li, Z. Y.; Shi, L.; Liu, X.; Li, H.; Han, S.; Chen, J.; Xu, G. *Cryst. Growth Des.* **2008**, *8*, 4440−4444.

(25) Yoo, S.-H.; Lee, J.-H.; Delley, B.; Soon, A. *Phys. Chem. Chem. Phys.* **2014**, *16*, 18570.

(26) Niu, W.; Zhang, L.; Xu, G. *ACS Nano* **2010**, *4*, 1987−1996.

(27) Watt, J.; Cheong, S.; Toney, M. F.; Ingham, B.; Cookson, J.; Bishop, P. T.; Tilley, R. D. *ACS Nano* **2010**, *4*, 396−402.

(28) Ramezani-Dakhel, H.; Mirau, P. A.; Naik, R. R.; Knecht, M. R.; Heinz, H. *Phys. Chem. Chem. Phys.* **2013**, *15*, 5488−5492.

(29) Sokoro, A.; Lehotay, D.; Eichhorst, J.; Treble, R. *J. Anal. Toxicol.* **2007**, *31*, 342−346.

(30) Bauskar, A. S.; Rice, C. A. *Electrochim. Acta* **2013**, *93*, 152−157.

(31) Fang, L.; Tao, Q.; Li, M.; Liao, L.; Chen, D.; Chen, Y. *Chin. J. Chem. Phys.* **2010**, *23*, 543−548.

(32) Vidakovic, T.; Christov, M.; Sundmacher, K. *Electrochim. Acta* **2007**, *52*, 5606−5613.